Chemical Science

ROYAL SOCIETY OF CHEMISTRY

EDGE ARTICLE

View Article Online
View Journal | View Issue

Cite this: *Chem. Sci.*, 2024, **15**, 2578

All publication charges for this article have been paid for by the Royal Society of Chemistry

Identifying the active sites and intermediates on copper surfaces for electrochemical nitrate reduction to ammonia†

Yohan Kim, ‡[a] Jinyoung Ko,‡[bc] Minyoung Shim, [a] Jiwon Park, [a] Hyun-Hang Shin,[d] Zee Hwan Kim, [d] Yousung Jung *[bc] and Hye Ryung Byon *[a]

Copper (Cu) is a widely used catalyst for the nitrate reduction reaction (NO_3RR), but its susceptibility to surface oxidation and complex electrochemical conditions hinders the identification of active sites. Here, we employed electropolished metallic Cu with a predominant (100) surface and compared it to native oxide-covered Cu. The electropolished Cu surface rapidly oxidized after exposure to either air or electrolyte solutions. However, this oxide was reduced below 0.1 V *vs.* RHE, thus returning to the metallic Cu before NO_3RR. It was distinguished from the native oxide on Cu, which remained during NO_3RR. Fast NO_3^- and NO reduction on the metallic Cu delivered 91.5 ± 3.7% faradaic efficiency for NH_3 at −0.4 V *vs.* RHE. In contrast, the native oxide on Cu formed undesired products and low NH_3 yield. Operando shell-isolated nanoparticle-enhanced Raman spectroscopy (SHINERS) analysis revealed the adsorbed NO_3^-, NO_2, and NO species on the electropolished Cu as the intermediates of NH_3. Low overpotential NO_3^- and NO adsorptions and favorable NO reduction are key to increased NH_3 productivity over Cu samples, which was consistent with the DFT calculation on Cu(100).

Received 31st October 2023
Accepted 4th January 2024

DOI: 10.1039/d3sc05793c

rsc.li/chemical-science

1. Introduction

Ammonia (NH_3) is imperative for agricultural fertilizers and hydrogen-carrying fuel.[1–3] However, the excessive use of artificial fertilizer has disrupted the nitrogen cycle, causing nitrates (NO_3^-) to drain into groundwater and rivers, and nitrous oxide (N_2O) emissions.[4–6] There is growing interest in using reactive nitrogen pollutants as an NH_3 source to address environmental concerns and explore clean energy alternatives. Electrochemical NO_3^- reduction reaction (NO_3RR) in water is the representative method, offering additional advantages over the Haber–Bosch process in terms of mild reaction conditions (room temperature, atmospheric pressure, and no need for natural gas feedstock),[7–12] and outperforming electrochemical N_2 reduction in kinetics.[13–15]

NO_3RR involves eight electron-transfer processes with a thermodynamic reduction potential (E^0) of +0.69 V *vs.* the reversible hydrogen electrode (RHE).[16–18]

$$NO_3^- + 9H^+ + 8e^- \rightarrow NH_3 + 3H_2O \; E^0 = 0.69 \text{ V } \textit{vs.} \text{ RHE}$$

Computational simulations envisioned a sequential deoxygenation process from NO_3^- to nitric oxide (*NO, where the asterisk symbol indicates surface adsorption of the species) or nitride (*N), followed by hydrogenation to yield NH_3.[18–20] Two key steps determine activity and selectivity; (i) the initial NO_3^- reduction to nitrite ($*NO_2$) is the rate-determining step. The sluggish process caused significant onset overpotential.[21,22] (ii) The *NO binding strength on the catalyst significantly impacts selective NH_3 production. Weak NO adsorption leads to NO dissolution or NO–NO coupling, yielding NO, N_2O, NH_2OH, or N_2 byproducts.[17,18,21–24]

Various catalysts have been investigated to optimize $*NO_3^-$ and *NO adsorption. Copper (Cu) emerges as the most economical choice in addition to its ability to create a significant potential gap between NO_3^- reduction and hydrogen evolution reaction (HER). Both Cu(111)[25–28] and (100) facets[9,29] exhibited reasonable activity in overall processes, and their performance was further enhanced when forming alloys or

[a]*Department of Chemistry, Korea Advanced Institute of Science and Technology (KAIST), 291, Daehak-ro, Yuseong-gu, Daejeon 34141, Republic of Korea. E-mail: hrbyon@kaist.ac.kr*

[b]*Department of Chemical and Biomolecular Engineering, Korea Advanced Institute of Science and Technology (KAIST), 291 Daehak-ro, Yuseong-gu, Daejeon 34141, Republic of Korea*

[c]*School of Chemical and Biological Engineering, Seoul National University, Seoul 08826, Republic of Korea. E-mail: yousung.jung@snu.ac.kr*

[d]*Department of Chemistry, Seoul National University, Seoul 08826, Republic of Korea*

† Electronic supplementary information (ESI) available. See DOI: https://doi.org/10.1039/d3sc05793c

‡ Contributed equally to this work.

bimetallic structures with Ru, Rh, Pd, or Ir.[11,30–34] However, the vulnerable nature of the Cu surface has posed challenges in identifying the actual active sites and their roles; the metallic Cu undergoes quick oxidation in the air or an electrolyte solution. Conversely, the Cu oxides are electrochemically reduced. However, degrees of oxidation and reduction vary depending on the conditions and have not been easily controlled. For instance, CuO nanostructures transformed into Cu/Cu_2O heterostructures through *in situ* reduction.[12] Although the heterostructure showed better NH_3 productivity, identifying the true active sites has proven difficult due to the presence of defect/strain structures with varying surface roughnesses[9,35–37] and the complexity of valence states at Cu/Cu_2O sites.[38]

Here, we focused on the Cu surface states that are essential as the active sites to determine NO_3RR activity and selectivity. Three surface states of Cu foil were prepared, representing the native oxide-covered Cu, partially etched native oxide, and metallic Cu surface with a predominant (100) facet. It was found that the metallic Cu surface was oxidized by air or electrolyte solution. However, this oxide layer was rapidly eliminated below 0.1 V *vs.* RHE (before starting NO_3RR). The reverted metallic Cu surface facilitated NO_3^- and NO reductions and offered 91.5 ± 3.7% of NH_3 faradaic efficiency at −0.4 V *vs.* RHE. In contrast, native oxide on Cu was not fully removed under the same electrochemical condition, providing inferior NH_3 productivity. *Operando* Raman spectroscopy analysis revealed $*NO_3^-$, $*NO_2$, and *NO species on metallic Cu as the intermediates of NH_3. Subsequent reductions of $*NO_3^-$ and *NO are associated with NH_3 productivity, which is further supported by the DFT calculation. In contrast, the native oxide on Cu did not clearly show these intermediates and appeared *NO with higher overpotential.

2. Results and discussion

We prepared three types of Cu foils using different surface treatments (Scheme S1 and Experimental details in ESI†). First, as-received Cu foil was washed with acetone, isopropanol, and de-ionized (DI) water sequentially using bath sonication for 5 min each. The resulting Cu foil was named w-Cu. The second and third methods eliminated the native oxide layer of w-Cu.[39,40] The w-Cu was soaked in glacial acetic acid for 5 min,[41] which was indicated as a-Cu. Separately, w-Cu was electrochemically polished by applying 2 V for 5 min in 85 wt% H_3PO_4 solution,[42,43] denoted as e-Cu. All these treatments were conducted just before surface characterizations or NO_3RR tests.

The as-received Cu surface state and morphology remained intact in w-Cu (Fig. 1a). Scanning electron microscope (SEM) and atomic force microscope (AFM) displayed stripe patterns on the Cu surface, attributed to root-mean-square (RMS) roughness at 14.4 nm in 100 μm^2 area. While a-Cu had a similar surface pattern, a surface RMS increased to 25.4 nm (Fig. 1b). It indicated non-uniform and incomplete surface etching. Electron backscatter diffraction (EBSD) analysis revealed a prevalent Cu(100) facet (red) over both w-Cu and a-Cu surfaces, while various polycrystals also appeared with small domains. Chemical analyses using Auger spectra (Fig. 1) and X-ray photoelectron spectroscopy (XPS, Fig. S1†) showed intense Cu^+ and Cu^{2+} signals for both samples, *i.e.*, the presence of Cu_2O and CuO.[44]

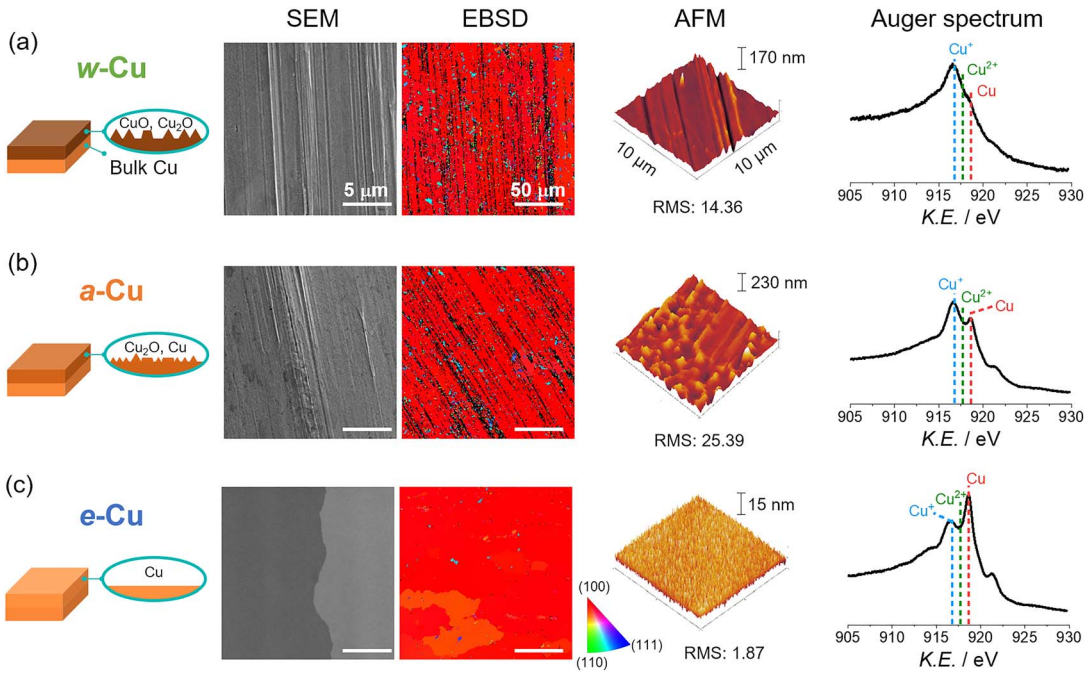

Fig. 1 Surface characteristics of Cu electrodes with different surface treatments through (a) solvent washing (top panel, w-Cu), (b) acid-etching (middle panel, a-Cu), and (c) electropolishing (bottom panel, e-Cu). Analyses of each sample showed schematic illustration, SEM image, electron backscatter diffraction (EBSD) image with a color indicator (right bottom), AFM image, and Auger Cu LMM spectrum (from the left to the right side). All scale bars in SEM and EBSD indicate 5 μm and 50 μm, respectively. RMS stands for root-mean-square roughness with nanometer unit. Dashed lines in Auger spectra indicate Cu^+ (916.8 eV), Cu^{2+} (917.7 eV), and Cu^0 (918.6 eV).

Quantitatively, the surface of w-Cu was covered by 81% Cu^{+} and 21% Cu^{2+} (Fig. S2†). There were no metallic Cu^{0} present in the Cu Auger spectra. In comparison, a-Cu had a partially metallic Cu surface (37%) due to etching, although the major species was Cu^{+} (63%). Native Cu oxide on w-Cu was further analysed using cross-sectional transmission electron microscopy (TEM), exhibiting CuO(111) and (002) with 0.23 and 0.25 nm *d*-spacings, respectively (Fig. 2a). The thicknesses were varied from 2 to 40 nm in multiple areas (Fig. 2b).

In contrast, e-Cu had a stripe-free and even surface with Cu(100) facet (RMS: 1.9 nm, Fig. 1c). Auger and XPS analyses identified the prevalent metallic Cu^{0} (71% coverage) on the surface, demonstrating the complete elimination of the oxide layer (Fig. S1 and S2†).

Three types of Cu foils were susceptible to oxidation when electrochemical cells were assembled in ambient air and stabilized in an electrolyte solution. Thus, the actual surface states before NO_3RR tests should be identified. We analysed Cu surfaces after air-tight H-cell installation (details in Fig. S3†)

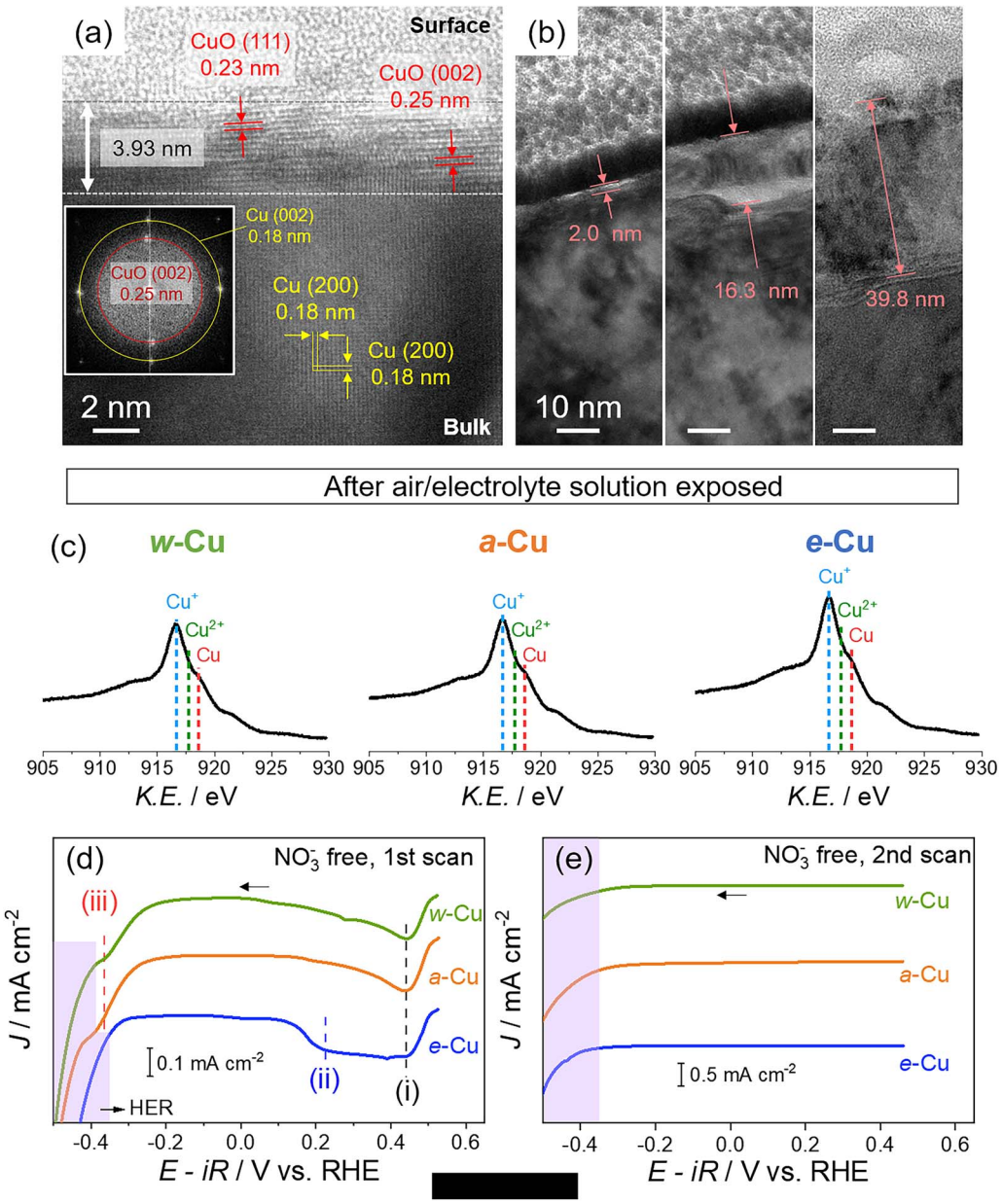

Fig. 2 Characteristics of native oxide on Cu foils and after air/electrolyte solution oxidation. (a and b) Cross-sectional TEM images of w-Cu in multiple areas, prepared by focused ion beam (FIB) milling. (a) *d*-spacing of CuO from native oxide and Cu(200) and corresponding FFT image (inset) (b) varied native oxide thicknesses of w-Cu. (c) Auger Cu LMM spectra of Cu foils after exposure to air and Ar-saturated 1 M KOH solution. (d and e) Cathodic linear sweep voltammogram (LSV) profiles of Cu foils in Ar-saturated 1 M KOH solutions. Potentials were swept from open circuit potential (0.53 V) for (d) the initial and (e) the second scan at a rate of 5 mV s^{-1}. The violet regions indicate hydrogen evolution reaction (HER).

and argon (Ar) gas purge into 1 M KOH solution for 10 min. Auger spectra revealed a growing Cu^+ signal on e-Cu and a-Cu compared to a negligible change on w-Cu (Fig. 2c), indicating immediate oxidation arising from the metallic Cu sites. We also note that residual organic contaminants appearing on w-Cu were removed by soaking in the KOH solution (Fig. S1 and S4†).

However, the instantly oxidized Cu differs from the native oxide; the former was rapidly removed before or during the initial NO_3RR tests. We tracked different reduction potentials of these oxide layers in 1 M KOH solution. Cathodic linear sweep voltammetry (LSV) in Fig. 2d shows three potential regions: (i) 0.4–0.5 V (*vs.* RHE unless otherwise stated), (ii) 0.1–0.4 V, and (iii) −0.25–−0.45 V. The (i) includes the CuO reduction to Cu_2O, and the (ii) and (ii) regions indicate $Cu(OH)_2/Cu_2O$ reduction to Cu^0.[45–47] The cathodic signal of CuO was developed in (i) for all samples. However, the $Cu(OH)_2/Cu_2O$ reduction in the (ii) region was applied for e-Cu only. With higher overpotentials (close to HER), the Cu^+ reduction appeared for a-Cu and w-Cu, but not e-Cu, as shown in (iii) region.[46,48–50] The appearance of the cathodic peaks in (iii) is, therefore, likely due to the thick native oxide (up to 40 nm).[45,46,48,49,51] During the second LSV scan, all oxide/hydroxide signals vanished (Fig. 2e). It indicates that the metallic Cu surface was recovered on e-Cu below 0.1 V, whereas the native oxide was reduced to below −0.4 V.

Next, NO_3RRs were examined with 50 mM KNO_3. Cathodic LSVs showed two waves for e-Cu and three for a-Cu and w-Cu (Fig. 3a–c). The initial (c_1) and second waves (c_2) appeared for all Cu foils, while the third one (c_3) at higher overpotentials only emerged for a-Cu and w-Cu (Fig. 3a–c). To identify each signal, NO_2^- or NO, which are key intermediates in NO_3RR, was added to a 1 M KOH solution without NO_3^-.[29] Adding 50 mM $NaNO_2$ vanished the c_1 wave, identifying c_1 to the NO_3^- reduction to NO_2/NO_2^-. NO gas was generated by Cu powder and neat nitric acid (HNO_3) reaction and introduced to the electrochemical cell through the Ar stream (Scheme S2†).[52] Emerging NO cathodic waves notably relied on the Cu surfaces; the metallic Cu on e-Cu promoted the NO reduction at c_2 (−0.02 V) with a significant current density (J), whereas the native Cu oxide of w-Cu reduced NO at c_3 (−0.31 V). The a-Cu allowed both c_2 (−0.10 V) and c_3 (−0.28 V) due to the coexistence of both metallic Cu and Cu oxide.[21] Consequently, metallic Cu offered more active sites for prompt NO reduction and caused the absence of c_3.

For the potential aspect, e-Cu offered more positive (*i.e.*, lower overpotentials) for c_1 (>100 mV) and c_2 (>50 mV) compared to those for a-Cu and w-Cu (Table 1). The rate-determining NO_3^- reduction to NO_2^- was significantly catalysed by the metallic Cu and improved overall reaction kinetics. Additionally, the Tafel slope of e-Cu was smaller (71.4 mV dec^{-1}) than that of a-Cu and w-Cu (>100 mV dec^{-1}) (Fig. S5†) and even superior to the ones of previously reported Cu-based catalysts (Table S1†).[21,38,53–57]

Furthermore, the active sites on e-Cu were stable. Cyclic voltammograms (CVs) exhibited constant NO-reducing waves during three cycles, although sample surfaces were roughened

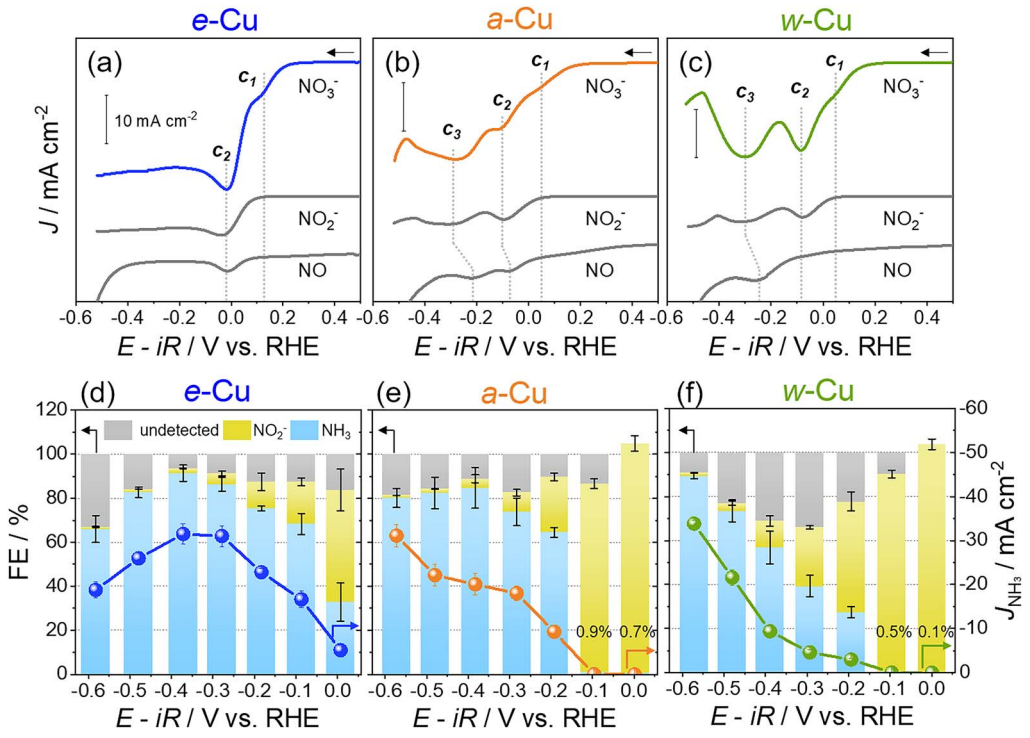

Fig. 3 Electrochemical NO_3RR for Cu foils in Ar-saturated 1 M KOH solutions with 50 mM KNO_3. (a–c) Cathodic LSVs for (a) e-Cu, (b) a-Cu, and (c) w-Cu at a scan rate of 5 mV s^{-1}. The c_1–c_3 indicate cathodic waves, and all scale bar indicates 10 mA cm^{-2}. NO_2^- and NO curves (gray) were acquired from 50 mM $NaNO_2$ and NO gas, respectively, instead of NO_3^-. (d–f) Potential-dependent faradaic efficiency (FE, bar graphs with the left y-axis) of NH_3 (sky blue), NO_2^- (pale yellow), and undetected products (gray) by colorimetric analyses for (d) e-Cu, (e) a-Cu, and (f) w-Cu. The partial current density of NH_3 (J_{NH_3}) is indicated as dots with the right y-axis.

Table 1 Evaluations of NO_3RR with different Cu foils

	Surface states Auger spectra	Cathodic potentials in LSV (V *vs.* RHE) | cathodic reactant(s) c_1[a]		c_2		c_3		FE_{NH_3} (%) 0 V	FE_{NH_3} (%) −0.4 V	Yield rate[b] (mass yield rate)[c] −0.4 V	EE_{NH_3} (%) −0.4 V
e-Cu	Cu^0 (71%)	0.15	NO_3^-	−0.02	NO_2^-, NO	NA	—	41.6	91.5	143.1 (2.43)	30.8
a-Cu	Cu^+ (63%)	0.05		−0.10	NO_2^-, NO	−0.28	NO	0.7	84.8	95.5 (1.62)	28.4
w-Cu	Cu^+ (81%)	0.03		−0.08	NO_2^-	−0.31	NO	0.1	56.9	43.8 (0.75)	19.0

[a] c_1 potentials were indicated from the 2nd derivatives of LSV curves. [b] The unit is μmol cm^{-2} h^{-1}. [c] The unit is mg cm^{-2} h^{-1}.

during NO_3RR (Fig. S6 and S7†). To depict electrochemical active surface area (ECSA), we estimated the roughness factors from two methods: the RMS surface roughness from the AFM measurement and the electric double layer capacitance (EDLC) relative to the specific capacitance, as shown in Table S2 and S3.† Both methods consistently resulted in the lowest roughness factor and ECSA for the as-prepared e-Cu. During NO_3RR, the EDLC of e-Cu increased more than a-Cu and w-Cu (Fig. S8a†). However, the geometric-area-normalized current densities were constant during CV cycling (Fig. S6†). In addition, e-Cu still exhibited the highest ECSA-normalized current density in the fourth cycled CV (Fig. S8 and Table S3†). It corroborated the stable and preserved active sites on e-Cu regardless of the increased surface roughness.

The selectivity and yield of NH_3 production was assessed by chronoamperometry (CA) tests and colorimetric analyses of the electrolyte solution (NO_2^- and NH_3 detection, Fig. S9–S11†).[12,18,21] For e-Cu, faradaic efficiency of NH_3 (FE_{NH_3}) was 41.6% at 0.0 V and maximized to 91.5% at −0.4 V during 1 h reaction (Fig. 3d). Isotope labeling tests demonstrated that NO_3^- was the exclusive N source to form NH_3 (Fig. S12†). Declining FE_{NH_3} below −0.4 V was attributed to HER included in the increased undetected species. By comparison, w-Cu and a-Cu generated <1% FE_{NH_3} at 0.0 V, where NO_2^- was the primary product (Fig. 3e and f). A very small current density hindered a precise quantification (>100% FE), and this result is explained by an insignificant current density at c_1 in the LSV (Fig. 2b and c). High charge-transfer resistances obtained at 0.0 V and −0.1 V also illustrated sluggish NO_3^- reduction on the native Cu oxide (Fig. S13†). At −0.4 V, although FE_{NH_3} was developed to 84.8% (a-Cu) and 56.9% (w-Cu), the efficiency was still inferior to e-Cu. We also found that the undetected species became the maximum at −0.3 V from w-Cu and decreased toward the negative potential, distinct from the e-Cu trend (Fig. 3f). Undesired products, such as N_2O, NH_2OH, and N_2, were produced from w-Cu (Fig. S14†) due to weak *NO adsorption on the native oxide.[58,59] A subsequent decline of undetected species indicated a slow HER from the oxide layer that was not wholly eliminated during NO_3RR. The a-Cu showed an in-between tendency as existing both Cu^0 and native oxide (Fig. 3e). Still, the contribution of metallic Cu for FE_{NH_3} was notable at −0.2–−0.4 V. As a result, e-Cu showed an excellent NH_3 yield rate and half-cell energy efficiency (Table 1 and Fig. S15†), verifying the best NH_3 selectivity.

To further shed light on the NO_3RR process, e-Cu and w-Cu surfaces were observed by *operando* electrochemical shell-isolated nanoparticle-enhanced Raman spectroscopy (SHINERS) using $Au@SiO_2$ nanoparticles and Nafion binder (Fig. 4a, S16 and S17, and details in ESI†). Spectra of as-prepared e-Cu and w-Cu surfaces showed peaks of Cu_2O (430 cm^{-1}), $Cu(OH)_x$ (489 cm^{-1}), and CuO (630 cm^{-1}) (the left panel of Fig. 4b, c and Table S4†). However, the oxide/hydroxide peaks from e-Cu weakened at 0.0–−0.2 V, validating a recovery of the metallic Cu surface during NO_3RR (Fig. S18†). The trend is more evident when comparing peak-height intensity with potential change, as shown in Fig. S18.† During NO_3RR, e-Cu showed that the peaks of $Cu(OH)_x$ and CuO were almost completely absent, while Cu_2O species exhibited a relatively small decrease. In sharp contrast, w-Cu preserved all oxide peaks in 0.0–−0.5 V. At the end of NO_3RR, the peaks of Cu oxides remained on w-Cu but not on e-Cu.

NO_3RR intermediates were observed in 900–1700 cm^{-1} region (the right panel of Fig. 4b, c and Table S5†), where peaks of Nafion binder and residual citrate used for the synthesis of Au nanoparticles (Fig. S19†) also appeared, marked as ● and ○, respectively. Before applying a potential, a strong symmetric stretching peak of NO_3^- ($\nu_s(NO_3^-)$, 1047 cm^{-1}) in the solution emerged. At 0.0 V, this intensity weakened on e-Cu, while asymmetric NO_2 of NO_3^- peak ($\nu_{as}(NO_2)$, 1354 cm^{-1})[60,61] was intensified, possibly due to $*NO_3^-$ adsorption (the right panel of Fig. 4b). Concurrently, peaks of $*NO_2$ intermediates were observed as the result of NO_3^- reduction,[9,35–37] assigned to ν_{as}(-*ONO*) (1290 cm^{-1}) and ν_{as}(*ON = O) (1367 cm^{-1}). More importantly, the appearance of *NO (1608 cm^{-1}) at 0.0–−0.1 V signified the suitable binding strength with e-Cu and the occurrence of subsequent hydrogenation. It caused the appearance of peaks of $*NH_2$ (δ_s(H*NH), 1320 cm^{-1}) at 0.0–−0.3 V and growing $*NH_3$ associated δ_{as}(H*NH) (1578 cm^{-1}) at −0.3 V. Rapid NH_3 production at −0.4 V then attenuated all Raman peak intensities, and HER obscured signals at −0.5 V.

In comparison, w-Cu showed intense peaks of $*NO_2$ (1367 cm^{-1} of *ON=O and 1450 cm^{-1} of *ON*=O) at 0.0–−0.2 V (the right panel of Fig. 4c). Unlike the e-Cu case, new hydrogenated species emerged, such as $\delta(NH_2)$ (1160 cm^{-1}) possibly arising from NH_2OH,[62] δ(*NH) (1520 cm^{-1}),[62,63] and δ(H*NO) (1534 cm^{-1}), with strong intensities. We presume that they are intermediates of byproducts (N_2O, NH_2OH, and N_2) rather than those of NH_3. Meanwhile, *NO had not yet emerged

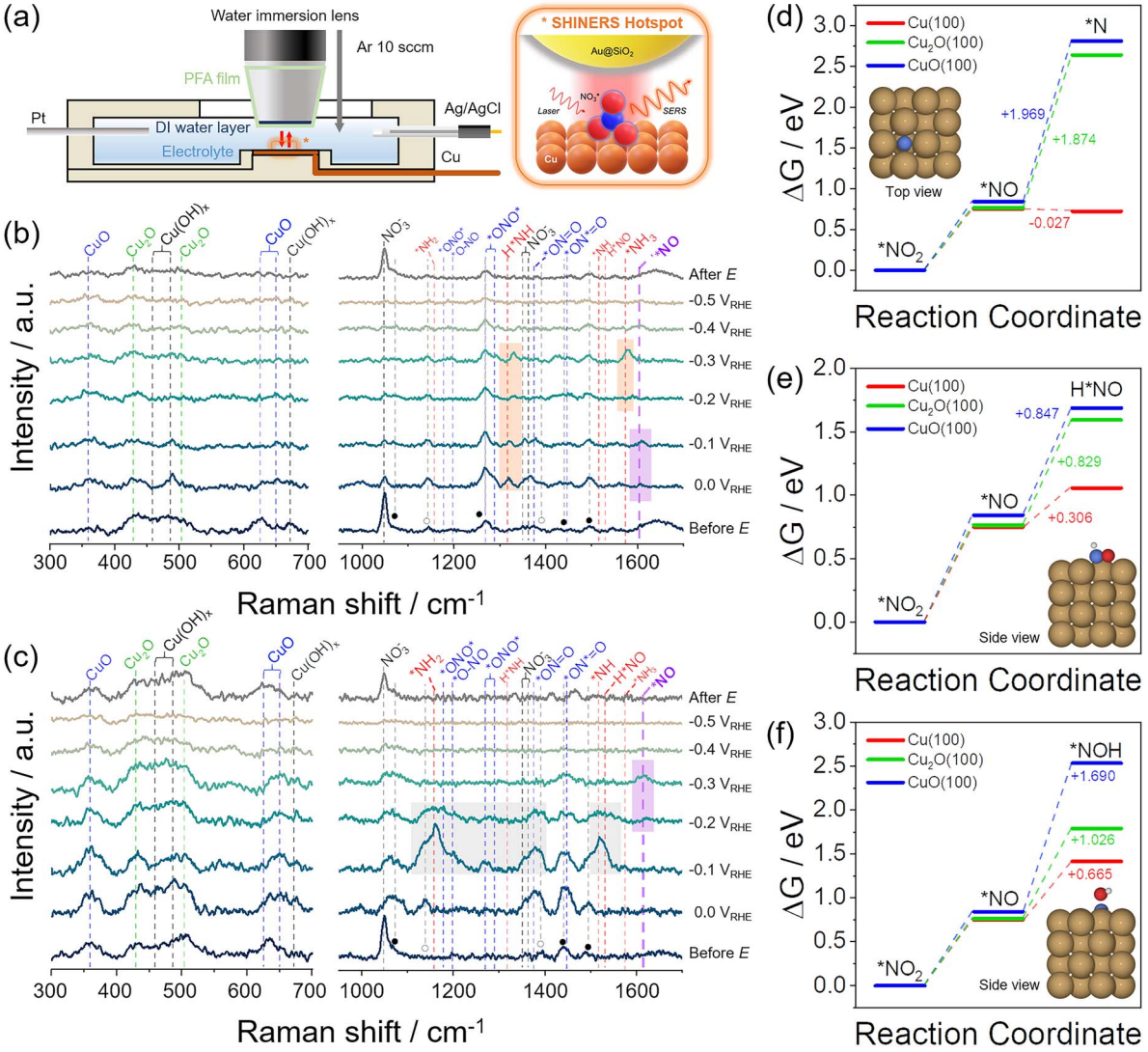

Fig. 4 *Operando* SHINERS analysis for NO_3^- reduction process on e-Cu and w-Cu electrodes. (a) Schematic illustration of an electrochemical cell. The right scheme illustrates the SERS hotspot defined by the SHIN ($Au@SiO_2$) particle placed on top of the Cu surface undergoing a chemical reaction. (b and c) SERS spectra for (b) e-Cu and (c) w-Cu, before the test, 0.0 V–−0.5 V *vs.* RHE, and after the test (from bottom to top). The potential was negatively scanned with −100 mV step. Vertical dashed lines indicate vibrational frequencies of CuO, Cu_2O, $Cu(OH)_x$, NO_3^- (black), NO_2^- (blue), NO (violet), HNO/NH/NH_2/NH_3 (red). For the details of peak assignment, see Tables S4 and S5.† The orange, violet, and gray box indicate *NH_2/*NH_3, *NO, and byproduct intermediates, respectively. (d–f) Reaction free energy diagrams of (d) *NO_2 → *N, (e) *NO_2 → H*NO, and (f) *NO_2 → *NOH on Cu(100), Cu_2O (100), and CuO(100) at pH = 14, calculated by DFT. The insets showed the optimized structures of three final intermediates adsorbed on Cu(100) (brown, blue, red, and white represent Cu, N, O, and H, respectively).

in this potential range, suggesting that the accessible NO is weakly absorbed on w-Cu or reacts undesirably with re-dissolved NO, which was supported by the increased undetected species in Fig. 3f. The apparent *NO peak was observed at −0.3 V, which aligned with the NO reduction potential (c_3) in the LSV (Fig. 3c) and the increased FE_{NH_3} below −0.3 V (Fig. 3f).

DFT calculations also supported the notable influence of the Cu valence state on *NO_2 and *NO reductions using three Cu surface models: Cu(100), Cu_2O(100), and CuO(100) (Fig. S20 and Computational details in ESI†). We first examined the formation of *NO from the reduction of *NO_2 and calculated Gibbs free energy changes (ΔG) on different Cu surfaces at pH = 14 (Tables S6–S8†). The ΔG value is positive on all Cu surfaces, implying a thermodynamically energy-consuming reduction process. However, each surface has only a small difference in ΔG, around 0.75 eV.

Subsequent reduction of *NO through the ΔG was calculated. Simulated intermediates were suggested as *N, H*NO, and *NOH,[11,18,64,65] which are different in deoxygenation, hydrogenation, and final product determination steps.[65–67] Fig. 4d–f shows each intermediate's Gibbs free energy diagrams on Cu surfaces at pH = 14. The optimized structures of three intermediates adsorbed on each surface were presented in the inset and Fig. S21–S23.† The Cu(100) surface had the most favourable ΔG value of −0.027 eV for forming *N from *NO. In comparison, the other oxide surfaces had significantly large

positive values (>1.8 eV) due to the thermodynamic barrier toward *N, which was suggested to be a highly NH_3-selective intermediate.[65] The ΔG for the formation of H*NO and *NOH are also calculated through *NO reduction. $Cu_2O(100)$ and CuO(100) surfaces showed the lowest ΔG for H*NO compared to *N and *NOH, consistent with the appearance of H*NO species in the Raman spectrum at −0.1−−0.2 V (Fig. 4c). Nonetheless, the energy barrier for H*NO and *NOH formation with *NO reduction was lower at the Cu(100) surface than at Cu oxides. It suggests that all intermediates from the *NO reduction can be produced more easily on the metallic Cu surface, consistent with the available experimental results.

3. Conclusions

In summary, we studied Cu surface states for NO_3RR activity and selectivity. The native oxide layer on Cu involved slow NO_3^- and NO reduction and produced undesired products. In contrast, metallic Cu with an even surface produced NH_3 with better activity and selectivity. Although the metallic Cu was immediately oxidized in air or electrolyte solution, this oxide was rapidly reduced below 0.1 V. Therefore, the metallic Cu^0 surface was recovered in contrast to the persistent native oxide. Electrochemical tests, operando Raman spectroscopy, and DFT calculations consistently demonstrated the metallic Cu as the active sites of NO_3RR, attributed to suitable $*NO_3^-$ and *NO adsorptions and following their rapid reductions.

Data availability

All data associated with this publication are provided in the ESI.†

Author contributions

Y. K. and H. R. B. designed the experiments; Y. K. and M. S. conducted electrochemical experiments; J. K. contributed to DFT calculations on free energy change under the supervision of Y. J.; J. P., H. S, and Z. H. K. advised to setup and interpret SHINERS experiments.; H. S. simulated the Raman peak position of intermediates under the supervision of Z. H. K; Y. K., H. R. B., J. K., and Y. J. wrote the manuscript.

Conflicts of interest

There are no conflicts to declare.

Acknowledgements

This work was supported by the National Research Foundation of Korea (NRF) grant funded by the Korean government (MSIT) (No. NRF-2019R1A2C2007551 and 2021R1A5A1030054).

Notes and references

1 J. G. Chen, R. M. Crooks, L. C. Seefeldt, K. L. Bren, R. M. Bullock, M. Y. Darensbourg, P. L. Holland, B. Hoffman, M. J. Janik, A. K. Jones, M. G. Kanatzidis, P. King, K. M. Lancaster, S. V. Lymar, P. Pfromm, W. F. Schneider and R. R. Schrock, *Science*, 2018, **360**, eaar6611.
2 G. Qing, R. Ghazfar, S. T. Jackowski, F. Habibzadeh, M. M. Ashtiani, C. P. Chen, M. R. Smith 3rd and T. W. Hamann, *Chem. Rev.*, 2020, **120**, 5437–5516.
3 X. Zhao, G. Hu, G. F. Chen, H. Zhang, S. Zhang and H. Wang, *Adv. Mater.*, 2021, **33**, e2007650.
4 D. E. Canfield, A. N. Glazer and P. G. Falkowski, *Science*, 2010, **330**, 192–196.
5 N. Gruber and J. N. Galloway, *Nature*, 2008, **451**, 293–296.
6 W. Battye, V. P. Aneja and W. H. Schlesinger, *Earth's Future*, 2017, **5**, 894–904.
7 Y. Wang, H. Li, W. Zhou, X. Zhang, B. Zhang and Y. Yu, *Angew Chem. Int. Ed. Engl.*, 2022, **61**, e202202604.
8 S. Cheon, W. J. Kim, D. Y. Kim, Y. Kwon and J.-I. Han, *ACS Energy Lett.*, 2022, **7**, 958–965.
9 Q. Hu, Y. Qin, X. Wang, Z. Wang, X. Huang, H. Zheng, K. Gao, H. Yang, P. Zhang, M. Shao and C. He, *Energy Environ. Sci.*, 2021, **14**, 4989–4997.
10 D. Kim, D. Shin, J. Heo, H. Lim, J.-A. Lim, H. M. Jeong, B.-S. Kim, I. Heo, I. Oh, B. Lee, M. Sharma, H. Lim, H. Kim and Y. Kwon, *ACS Energy Lett.*, 2020, **5**, 3647–3656.
11 Y. Wang, A. Xu, Z. Wang, L. Huang, J. Li, F. Li, J. Wicks, M. Luo, D. H. Nam, C. S. Tan, Y. Ding, J. Wu, Y. Lum, C. T. Dinh, D. Sinton, G. Zheng and E. H. Sargent, *J. Am. Chem. Soc.*, 2020, **142**, 5702–5708.
12 Y. Wang, W. Zhou, R. Jia, Y. Yu and B. Zhang, *Angew Chem. Int. Ed. Engl.*, 2020, **59**, 5350–5354.
13 H. Hirakawa, M. Hashimoto, Y. Shiraishi and T. Hirai, *ACS Catal.*, 2017, **7**, 3713–3720.
14 J. Wu, J.-H. Li and Y.-X. Yu, *J. Phys. Chem. Lett.*, 2021, **12**, 3968–3975.
15 A. Stirling, P. Imre and J. Mink, *J. Chem. Phys.*, 1994, **100**, 2910.
16 B. Min, Q. Gao, Z. Yan, X. Han, K. Hosmer, A. Campbell and H. Zhu, *Ind. Eng. Chem. Res.*, 2021, **60**, 14635–14650.
17 Z. Wang, D. Richards and N. Singh, *Catal. Sci. Technol.*, 2021, **11**, 705–725.
18 H. Wan, A. Bagger and J. Rossmeisl, *Angew Chem. Int. Ed. Engl.*, 2021, **60**, 21966–21972.
19 J.-X. Liu, D. Richards, N. Singh and B. R. Goldsmith, *ACS Catal.*, 2019, **9**, 7052–7064.
20 R. Yang, H. Li, J. Long, H. Jing, X. Fu and J. Xiao, *ACS Sustain. Chem. Eng.*, 2022, **10**, 14343–14350.
21 G. E. Dima, A. C. A. de Vooys and M. T. M. Koper, *J. Electroanal. Chem.*, 2003, **554–555**, 15–23.
22 Y. Zeng, C. Priest, G. Wang and G. Wu, *Small Methods*, 2020, **4**, 2000672.
23 Y. Wang and J. Qu, *Water Environ. Res.*, 2006, **78**, 724–729.
24 J. Long, C. Guo, X. Fu, H. Jing, G. Qin, H. Li and J. Xiao, *J. Phys. Chem. Lett.*, 2021, **12**, 6988–6995.
25 D. P. Butcher and A. A. Gewirth, *Nano Energy*, 2016, **29**, 457–465.

26 X. Fu, X. Zhao, X. Hu, K. He, Y. Yu, T. Li, Q. Tu, X. Qian, Q. Yue, M. R. Wasielewski and Y. Kang, *Appl. Mater. Today*, 2020, **19**, 100620.
27 S.-E. Bae and A. A. Gewirth, *Faraday Discuss.*, 2008, **140**, 113–123.
28 K. Wu, C. Sun, Z. Wang, Q. Song, X. Bai, X. Yu, Q. Li, Z. Wang, H. Zhang, J. Zhang, X. Tong, Y. Liang, A. Khosla and Z. Zhao, *ACS Mater. Lett.*, 2022, **4**, 650–656.
29 E. Pérez-Gallent, M. C. Figueiredo, I. Katsounaros and M. T. M. Koper, *Electrochim. Acta*, 2017, **227**, 77–84.
30 F. Y. Chen, Z. Y. Wu, S. Gupta, D. J. Rivera, S. V. Lambeets, S. Pecaut, J. Y. T. Kim, P. Zhu, Y. Z. Finfrock, D. M. Meira, G. King, G. Gao, W. Xu, D. A. Cullen, H. Zhou, Y. Han, D. E. Perea, C. L. Muhich and H. Wang, *Nat. Nanotechnol.*, 2022, **17**, 759–767.
31 W. Gao, K. Xie, J. Xie, X. Wang, H. Zhang, S. Chen, H. Wang, Z. Li and C. Li, *Adv. Mater.*, 2023, **35**, e2202952.
32 H. Liu, X. Lang, C. Zhu, J. Timoshenko, M. Ruscher, L. Bai, N. Guijarro, H. Yin, Y. Peng, J. Li, Z. Liu, W. Wang, B. R. Cuenya and J. Luo, *Angew Chem. Int. Ed. Engl.*, 2022, **61**, e202202556.
33 M. A. Akram, B. Zhu, J. Cai, S. Qin, X. Hou, P. Jin, F. Wang, Y. He, X. Li and L. Feng, *Small*, 2023, **19**, e2206966.
34 Q. Gao, H. S. Pillai, Y. Huang, S. Liu, Q. Mu, X. Han, Z. Yan, H. Zhou, Q. He, H. Xin and H. Zhu, *Nat. Commun.*, 2022, **13**, 2338.
35 Y. Xu, M. Wang, K. Ren, T. Ren, M. Liu, Z. Wang, X. Li, L. Wang and H. Wang, *J. Mater. Chem. A*, 2021, **9**, 16411–16417.
36 L. Fang, S. Wang, C. Song, S. Lu, X. Yang, X. Qi and H. Liu, *Chem. Eng. J.*, 2022, **446**, 137341.
37 Z. Shen, Y. Yu, Z. Zhao, S. Zhang, S. Xu, S. Yang and Y. Hu, *J. Hazard. Mater.*, 2023, **445**, 130651.
38 C. Wang, F. Ye, J. Shen, K.-H. Xue, Y. Zhu and C. Li, *ACS Appl. Mater. Interfaces*, 2022, **14**, 6680–6688.
39 T. Jang, J.-H. Kang, S. Kim, M. Shim, J. Lee, J. Song, W. Kim, K. Ryu and H. R. Byon, *ACS Appl. Energy Mater.*, 2021, **4**, 2644–2651.
40 P. Keil, D. Lützenkirchen-Hecht and R. Frahm, *AIP Conf. Proc.*, 2007, **882**, 490–492.
41 K. L. Chavez and D. W. Hess, *J. Electrochem. Soc.*, 2001, **148**, G640–G643.
42 K. Jiang, Y. Huang, G. Zeng, F. M. Toma, W. A. Goddard and A. T. Bell, *ACS Energy Lett.*, 2020, **5**, 1206–1214.
43 T. Kim and G. T. R. Palmore, *Nat. Commun.*, 2020, **11**, 3622.
44 S. Poulston, P. M. Parlett, P. Stone and M. Bowker, *Surf. Interface Anal.*, 1996, **24**, 811–820.
45 S. D. Giri and A. Sarkar, *J. Electrochem. Soc.*, 2016, **163**, H252–H259.
46 Y. Oh, J. Park, Y. Kim, M. Shim, T.-S. Kim, J. Y. Park and H. R. Byon, *J. Mater. Chem. A*, 2021, **9**, 11210–11218.
47 F. Caballero-Briones, J. M. Artés, I. Díez-Pérez, P. Gorostiza and F. Sanz, *J. Phys. Chem. C*, 2009, **113**, 1028–1036.
48 M. A. Hossain, R. Al-Gaashani, H. Hamoudi, M. J. Al Marri, I. A. Hussein, A. Belaidi, B. A. Merzougui, F. H. Alharbi and N. Tabet, *Mater. Sci. Semicond. Process.*, 2017, **63**, 203–211.
49 G. Iijima, T. Inomata, H. Yamaguchi, M. Ito and H. Masuda, *ACS Catal.*, 2019, **9**, 6305–6319.
50 S. Nakayama, T. Notoya and T. Osakai, *Anal. Sci.*, 2012, **28**, 323–331.
51 S. Nakayama, T. Notoya and T. Osakai, *J. Electrochem. Soc.*, 2010, **157**, C289–C294.
52 J. Choi, H.-L. Du, C. K. Nguyen, B. H. R. Suryanto, A. N. Simonov and D. R. MacFarlane, *ACS Energy Lett.*, 2020, **5**, 2095–2097.
53 W. He, J. Zhang, S. Dieckhofer, S. Varhade, A. C. Brix, A. Lielpetere, S. Seisel, J. R. C. Junqueira and W. Schuhmann, *Nat. Commun.*, 2022, **13**, 1129.
54 W. Lin, E. Zhou, J. F. Xie, J. Lin and Y. Wang, *Adv. Funct. Mater.*, 2022, **32**, 2209464.
55 O. Q. Carvalho, S. R. S. Jones, A. E. Berninghaus, R. F. Hilliard, T. S. Radniecki and K. A. Stoerzinger, *Electrochem. Sci. Adv.*, 2022, e210020.
56 J. Li, J. Gao, T. Feng, H. Zhang, D. Liu, C. Zhang, S. Huang, C. Wang, F. Du, C. Li and C. Guo, *J. Power Sources*, 2021, 511.
57 S.-E. Bae, K. L. Stewart and A. A. Gewirth, *J. Am. Chem. Soc.*, 2007, **129**, 10171–10180.
58 T. Feng, J. Wang, Y. Wang, C. Yu, X. Zhou, B. Xu, K. László, F. Li and W. Zhang, *Chem. Eng. J.*, 2022, **433**, 133495.
59 J. Zhou, F. Pan, Q. Yao, Y. Zhu, H. Ma, J. Niu and J. Xie, *Appl. Catal., B*, 2022, **317**, 121811.
60 S. G. Ramesh, S. Re, J. Boisson and J. T. Hynes, *J. Phys. Chem. A*, 2010, **114**, 255–1269.
61 M. H. Brooker and D. E. Irish, *Can. J. Chem.*, 1968, **46**, 229–233.
62 M. Wang, S. Liu, H. Ji, T. Yang, T. Qian and C. Yan, *Nat. Commun.*, 2021, 12.
63 S. Liu, T. Qian, M. Wang, H. Ji, X. Shen, C. Wang and C. Yan, *Nat. Catal.*, 2021, **4**, 322–331.
64 T. Hu, C. Wang, M. Wang, C. M. Li and C. Guo, *ACS Catal.*, 2021, **11**, 14417–14427.
65 O. Q. Carvalho, R. Marks, H. K. K. Nguyen, M. E. Vitale-Sullivan, S. C. Martinez, L. Arnadottir and K. A. Stoerzinger, *J. Am. Chem. Soc.*, 2022, **144**, 14809–14818.
66 Y. Wang, X. Qin and M. Shao, *J. Catal.*, 2021, **400**, 62–70.
67 M. Yang, Z. Wang, D. Jiao, G. Li, Q. Cai and J. Zhao, *Appl. Surf. Sci.*, 2022, **592**, 153213.